Appl. Math. Mech. -Engl. Ed., **43**(9), 1449–1468 (2022)

APPLIED MATHEMATICS AND MECHANICS (ENGLISH EDITION)

https://doi.org/10.1007/s10483-022-2898-6

Effects of size and location of distal tear on hemodynamics and wave propagation in type B aortic dissection*

Huimin CHEN[1], Qingzhuo CHI[1], Ying HE[1,†], Lizhong MU[1], Yong LUAN[2]

1. Key Laboratory of Ocean Energy Utilization and Energy Conservation of Ministry of Education, School of Energy and Power Engineering, Dalian University of Technology, Dalian 116024, Liaoning Province, China;
2. Department of Anesthesiology, The First Affiliated Hospital of Dalian Medical University, Dalian 116011, Liaoning Province, China

(Received Dec. 31, 2021 / Revised Jul. 5, 2022)

Abstract The type B aortic dissection (TBAD) is a perilous disease with high morbidity and mortality rates. The hemodynamics of TBAD in different scenarios has been widely studied by computational fluid dynamics (CFD) research. However, the flow pattern and wave propagation characteristics in the cardiovascular system with TBAD are not yet clear, and the effect of the distal tear is still unknown. In this work, a one-dimensional (1D) cardiovascular system model coupling with a zero-dimensional (0D) lumped-parameter model is introduced to study the hemodynamics and wave propagation in the cardiovascular system. The results show that the proposed 0D-1D method well captures the oscillation and retrograde characteristics for the flow in the false lumen (FL), and the smaller distal tear damps the retrograde flow. Besides, the distal tear should also be paid attention to, and the wave intensity (WI) can be used as an access mark of the degree of the aortic dissection (AD).

Key words type B aorta dissection (TBAD), zero-dimensional (0D)-one-dimensional (1D) coupling model, distal tear, flow pattern, wave intensity analysis (WIA)

Chinese Library Classification O357
2010 Mathematics Subject Classification 76D05

1 Introduction

The complicated type B aortic dissection (TBAD) is manifested by the threatened rupture, insufficient perfusion of organs, recurrent pain, hypertension, and early expansion. TBAD patients with acute renal failure and mesenteric ischemia may suffer increased mortality. The current preferred treatment option is thoracic endovascular aortic repair (TEVAR), which covers the entry tear with stent-graft, preventing the blood flow into the false lumen (FL) and elevating

* Citation: CHEN, H. M., CHI, Q. Z., HE, Y., MU, L. Z., and LUAN, Y. Effects of size and location of distal tear on hemodynamics and wave propagation in type B aortic dissection. *Applied Mathematics and Mechanics* (*English Edition*), **43**(9), 1449–1468 (2022) https://doi.org/10.1007/s10483-022-2898-6

† Corresponding author, E-mail: heying@dlut.edu.cn

Project supported by the National Natural Science Foundation of China (No. 51976026) and the Fundamental Research Funds of Central Universities of China (Nos. DUT22YG206 and DUT21JC25)

the long-term outcome of TBAD[1]. However, after TEVAR, there will be true lumen (TL) remodeling, and even a retrograde type A aortic dissection (TAAD) will occur[1]. For multi-tear scenarios, after TEVAR, the distal tears are not covered by the stent-graft. The effect of distal tears on hemodynamics may be more sophisticated. This implies that the geometric features of the tears, such as size and position, are associated with hemodynamics, which infers further progression of aortic dissection (AD) and complications.

The roles of the primary intimal tear in predicting the formation and development of AD and its complications have been widely investigated. Rudenick et al.[2] reported that the large entry tear led to higher diastolic pressure in FL. Evangelista et al.[3] indicted a poorer clinical outcome for large entry tears. Tsai et al.[4] showed that the smaller proximal tear and the lack of the distal tear resulted in a higher systolic FL pressure. Weiss et al.[5] showed that the entry tear in the aortic arch concavity and the short distance between the entry tear and the left subclavian artery were frequently associated with the further development of acute TBAD. Chi et al.[6] showed that the oscillatory index in aortic arch concavity was abnormally high in pre-tearing AD patients. Al-Kalei et al.[7] found that the primary intimal tear located in the distal convexity might be more likely to develop retrograde (TAAD). However, the roles of distal tears on hemodynamics have not been fully understood yet.

Computational fluid dynamics (CFD) has been increasingly used in hemodynamics research. Three-dimensional (3D) simulation is a potential method to aid clinical decision-making for interventional surgeries, and can give the detailed hemodynamics parameters in vessels[8–9]. However, it is typically conducted to analyze the local hemodynamic characteristics in vessels, and requires a lot of computational time. As an alternative method, a lumped model is put forward in AD simulation[10], which costs much less computational time. In addition, one-dimensional (1D) models have been widely used to analyze the waveform propagation in the cardiovascular system[11–13].

1D cardiovascular system models are based on the Navier-Stokes equations reduced by the rotational symmetry of vessels. The 1D model roots in the pulse wave analysis in the cardiovascular system are developed maturely by a coupling stenosis model[14] or lumped parameter heart model[15–16]. Different from open-loop 1D models, a closed-loop multi-scale zero-dimensional (0D)-1D cardiovascular model can simulate the entire circulation, including the coronary, cerebral arterial, and venous networks apart from the main artery trees[17]. 1D modeling also presents its powerful capacity of investigating the cardiovascular system, e.g., coronary, Fontan circulation, and pulmonary circulation[18]. Various methods for the treatment of boundary conditions have also been developed. Coccarelli et al.[19] presented a novel method by coupling a poro-elastic tube model representing the resistance of microcirculation. Nowadays, it has been developed for personalized analyses[20]. However, 1D modeling has not been applied to AD simulation. Several image-based lumped-parameter models have shown their potentials in giving fast and reasonable results for AD simulation[10, 21]. For AD scenarios, 1D modeling can provide a global view of hemodynamics and provide a good balance between accuracy and computational cost[12, 15]. Additionally, wave intensity analysis (WIA) can be performed based on the obtained waveforms from 1D simulation to give insight into the influence of wave propagation in circulation[20,22–23]. The simulated waveforms can be separated to forward and backward waves, representing the wave from the left ventricular ejection and the accumulative reflected wave from the peripheral vessels, respectively[22, 24]. Thus, not only the cumulative effect of the reflected wave from the peripheral vessels, FL, and tears can be clearly seen by the WIA, but also the ejection characteristics of the left ventricle can be investigated. In view of the computational cost, the precision, and the global view, a 0D-1D coupling model may be a good choice for studying hemodynamics in AD.

For the purpose of capturing the effects of the tears and FL on the cardiovascular system locally and globally, we implement a 0D-1D coupling cardiovascular system model based on a mature 1D artery tree model. By remodeling the AD model from the computed tomography

(CT) data, the geometry parameters are collected. The flow characteristics and pressure waves in the main arteries with different re-entry tear sizes of AD and its locations are investigated. The 1D personalized simulation results are validated against the magnetic resonance imaging (MRI) measured data. Section 2 presents the methodology of 1D modeling. After giving the validation in Section 3 and setting the data for AD simulation in Section 4, the detailed simulated results are presented in Section 5. The clinic implications and limitations of the modeling are discussed in Section 6 and Section 7, respectively. Finally, conclusions are drawn.

2 Methodology

2.1 Geometric parameters of the cardiovascular system with TBAD

Due to the reduction of dimension to the cardiovascular system, in the 0D-1D coupling model, only the volume of FL, the length of FL, the area of the cumulative tear, and the position of the tear are needed. Five CT samples of TBAD are preprocessed in the commercial software Simpleware ScanIP$^{\mathrm{TM}}$ to reconstruct the aorta and the main branches. The reconstructed model is given in Fig. 1(a), and the volume of the FL, the TL we measured, and the centerlines of the aorta and the branches are extracted. As shown in Fig. 1(b), owing to the existence of the tear, the TL and FL are connected by two pathways intersecting the centerline of the TL with two points corresponding to the entry and the re-entry positions, respectively. Thus, the length of FL can be determined by the distance of the two points. After measuring the volume of FL, the equivalent radius and length of the ideal cylindrical FL tube are determined, of which the process is shown in Figs. 1(c) and 1(d). The equivalent radius R_{eq} of FL is defined by the volume of FL V_{FL} and the length of FL L_{FL} via

$$R_{\mathrm{eq}} = \sqrt{V_{\mathrm{FL}}/(\pi L_{\mathrm{FL}})}.$$

The reconstructed 3D vascular models are as shown in Figs. 1(e) and 1(f), and the geometric parameters are listed in Table 1.

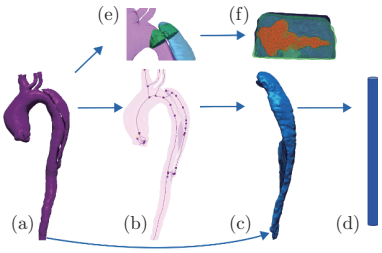

Fig. 1 (a) Reconstructed aortic model. (b) Extracted centerlines. (c) Extracted FL. (d) Equivalent FL. (e) One part of the 3D model including the tear. (f) Area of the tear in ANSYS SpaceClaim. The aorta models are reconstructed in SpaceClaim shown in (a). Then, the part of the model including the tear (e) is extracted and input to SpaceClaim to measure the area of the tear (f). Similarly, the length of FL is gauged by the centerline length shown in (b), and the volume of FL (c) is measured in Simpleware (color online)

From Table 1, it can be seen that the samples can be divided into two groups according to the AD severity. One is with large volume and long length of FL, while the other is with small volume and short length of FL. Additionally, the entry and re-entry sizes show three different patterns, i.e., the entry size is larger than, equal to, and smaller than the re-entry one. Therefore, the geometric data of AD in our simulation are set according to the characteristics and the average values of the data in Table 1.

Table 1 Geometric parameters of the FL measured in the reconstructed 3D model

Sample	Area of entry/mm^2	Area of re-entry/mm^2	Volume of FL/mm^3	Length of FL/mm	Equivalent radius of FL/mm
AD1	241.459 3	128.358 5	55 934.53	251.789	8.410 0
AD2	169.445 5	11.438 5	59 190.87	156.275	10.980 0
AD3	70.290 5	69.039 3	47 142.57	275.755	7.376 8
AD4	112.477 8	117.153 2	244 000.00	539.150	12.000 0
AD5	42.755 5	93.345 0	208 600.00	422.835	12.531 3
Average	127.285 7	83.866 9	–	–	10.259 6

2.2 1D modeling of the arterial tree

2.2.1 Geometric parameter

In the 1D model, arteries are assumed as a rotationally symmetric taper elastic tube. The cross-sectional radius of arteries varies exponentially with the axial distance x,

$$r(x) = r_{\mathrm{t}} \exp\left(\frac{x}{L} \log \frac{r_{\mathrm{b}}}{r_{\mathrm{t}}}\right), \tag{1}$$

where L is the length of each artery, r_{t} is the top cross-sectional radius of the artery, and r_{b} is the bottom cross-sectional radius of the artery. The details of the three parameters are listed in Table 2[14, 25]. The topology and the indices of the arteries are shown in Fig. 2.

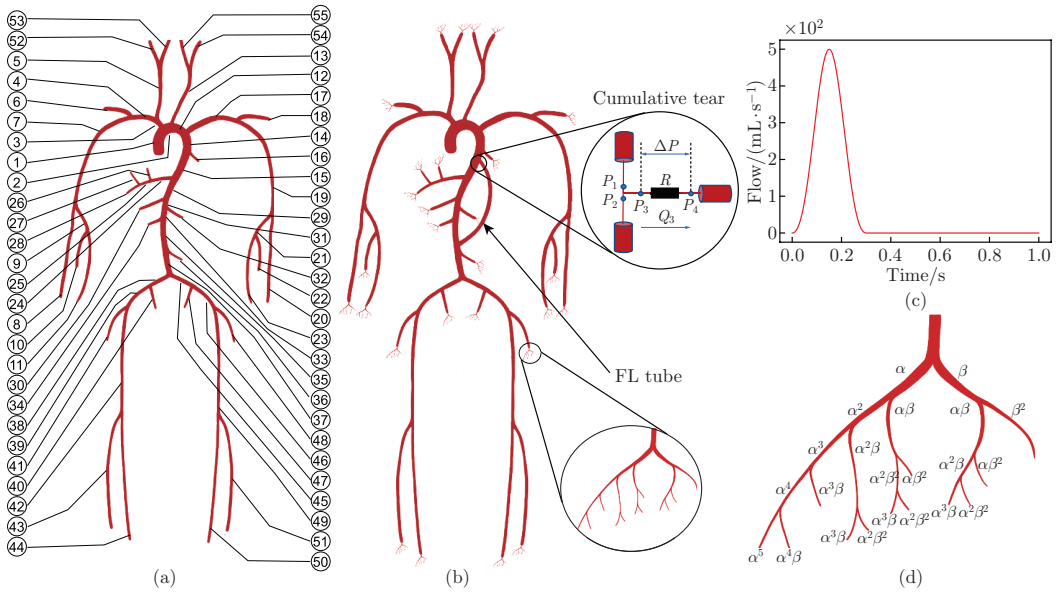

Fig. 2 Diagrams of the 1D model and 0D-1D coupling model used in this work. (a) 1D model using 55 main arteries and their order. (b) Added FL tube, 0D tear model, and structure tree models at terminal vessels. (c) Inlet flow profile used for simulation. (d) Structure tree model used for the outflow condition, in which the radii of the daughter arteries are reduced by the multiplication factors of α and β based on the radius of their parent artery (color online)

2.2.2 Governing equations

With the rotational symmetry assumption, the blood flows in the arteries can be expressed in a 1D form with the following continuity and momentum equations[11–12]:

$$\frac{\partial A}{\partial t} + \frac{\partial Q}{\partial x} = 0, \tag{2}$$

$$\frac{\partial Q}{\partial t}+\frac{\partial}{\partial x}\Big(\alpha\frac{Q^2}{A}\Big)+\frac{A}{\rho}\frac{\partial P}{\partial x}+K_r\frac{Q}{A}=0, \tag{3}$$

where t is the time. x is the axial direction of the artery. A, Q, and P denote the cross-sectional area, the volumetric flow rate, and the pressure, respectively. α is the Coriolis coefficient. When $\alpha=4/3$, the velocity variation shows a Poiseuille profile[15–16]. In practice, the profile is flat. In this model, α is set as 1. K_r is the friction force per unit length, and is set to $22\pi\nu$ (ν is the kinematic viscosity) in this model[12, 17].

The system of Eqs. (2) and (3) is closed by adding a state equation as follows[11–12]:

$$P-P_0=\frac{Eh}{r_0(1-\sigma^2)}\Big(\sqrt{\frac{A}{A_0}}-1\Big), \tag{4}$$

where P_0 is the reference pressure corresponding to the unstressed cross-sectional area A_0, and is defined as the lowest pressure during the diastolic phase between 7 135 Pa and 11 305 Pa[25]. E is Young's modulus. h is the wall thickness. r_0 is the radius of an artery. σ is Poisson's ratio, and is set to be 0.5 for vascular wall properties[25–26].

The values of E, h, and r_0 in the state equation are determined by[25]:

$$\frac{Eh}{r_0}=k_1\exp(k_2r_0)+k_3, \tag{5}$$

where

$$k_1=2.00\times10^7\,\mathrm{g\cdot s^{-2}\cdot cm^{-1}},\quad k_2=-22.53\,\mathrm{cm^{-1}},\quad k_3=8.65\times10^5\,\mathrm{g\cdot s^{-2}\cdot cm^{-1}}.$$

2.2.3 Inflow condition

A flow profile, with a single peak at the systolic period, is used at the inlet of ascending aorta. In order to implement WIA, only one peak in the systolic period is considered, and the systolic period t_s is taken as 0.3 s. The inlet flow profile shown in Fig. 2(c) is expressed by[27]

$$Q(t)=\begin{cases}Q_{\max}(0.251+0.290(\cos(\theta)+0.97\cos(2\theta)+0.47\cos(3\theta)+0.14\cos(4\theta))), & t\leqslant t_\mathrm{s},\\ 0, \quad \text{else}, \end{cases} \tag{6}$$

where $\theta=3\pi t-\sqrt{2}$. $Q_{\max}$ is the peak value of the flow profile in ascending aorta which is the MRI data in the literature[17, 28]. In our simulation, $Q_{\max}$ is set to be $500\,\mathrm{mL\cdot s^{-1}}$.

In this situation, the second peak, generated by the joint effect of the left ventricular relaxation and aortic contraction, is neglected. Therefore, the backward wave only denotes the reflection. Despite the simplified inlet flow profile, the shape is basically similar to the profile of the MRI measured data[28].

2.2.4 Bifurcation condition

The structure of the main artery tree is supposed to be a bifurcation tree from proximal to distal (see Fig. 2(a)). At a branching point, as the pressure and flow are continuous, the boundary conditions at the bifurcation can be written as

$$P_\mathrm{p}=P_\mathrm{d1}=P_\mathrm{d2},\quad Q_\mathrm{p}=Q_\mathrm{d1}+Q_\mathrm{d2}, \tag{7}$$

where p, d1, and d2 represent the parent vessel, the left daughter vessel, and the right daughter vessel, respectively. In view of the pressure continuity, the equality conditions for static pressure are assigned with neglecting the influence of dynamic pressure to avoid stability problems in the computation[15].

Table 2 Geometric parameters in the 1D cardiovascular system

No.	Artery	L/cm	r_{t}/cm	r_{b}/cm
1	Ascending aorta	4.00	1.525	1.420
2	Aortic arch A	3.00	1.420	1.342
3	Brachiocephalic	3.50	0.950	0.700
4,17	Right & left subclavian	3.50	0.425	0.407
5	Right common carotid	16.75	0.525	0.400
6,18	Right & left vertebral	13.50	0.200	0.200
7,19	Right & left brachial	39.75	0.407	0.250
8,20	Right & left radial	22.00	0.175	0.175
9,21	Right & left ulnar A	17.00	0.200	0.200
10,22	Right & left ulnar B	22.25	0.175	0.175
11,23	Right & left interosseus	7.00	0.100	0.100
12	Aortic arch B	4.00	1.342	1.246
13	Left common carotid	19.25	0.525	0.400
14	Thoracic aorta A	5.50	1.246	1.124
15	Thoracic aorta B	10.50	1.124	0.924
16	Intercostal	7.25	0.630	0.500
24	Celiac axis	2.00	0.350	0.300
25	Hepatic A	2.00	0.300	0.250
26	Hepatic B	6.50	0.275	0.250
27	Gastric	5.75	0.175	0.150
28	Splenic	5.50	0.200	0.200
29	Abdominal aorta A	5.25	0.924	0.838
30	Superior mesenteric	5.00	0.400	0.350
31	Abdominal aorta B	1.50	0.838	0.814
32,34	Right & left renal	3.00	0.275	0.275
33	Abdominal aorta C	1.50	0.814	0.792
35	Abdominal aorta D	12.50	0.792	0.627
36	Inferior mesenteric	3.75	0.200	0.175
37	Abdominal aorta E	8.00	0.627	0.550
38,45	Right & left external iliac	5.75	0.400	0.370
39,46	Right & left femoral A	14.50	0.370	0.314
40,47	Right & left internal iliac	4.50	0.200	0.200
41,48	Right & left deep femoral	11.25	0.200	0.200
42,49	Right & left femoral B	44.25	0.314	0.200
43,50	Right & left anterior tibial	32.00	0.125	0.125
44,51	Right & left posterior tibial	32.00	0.125	0.125
52,54	Right & left internal carotid	15.75	0.275	0.275
53,55	Right & left external carotid	15.75	0.275	0.275

2.2.5 Outflow condition

The 1D arterial system model is generally truncated at the end of the peripheral arteries, where the windkessel (WK) model and the structure tree (ST) model are used to express the flow behaviors in distal vasculatures. The WK model is a general outflow condition[12], while the ST model is analogous to the terminal artery for its dense bifurcation feature[25]. Since the whole main 55 arteries are considered, every terminal artery has its own geometry, the ST model is more capable of capturing a high frequency content of terminal impedance than the WK model[26]. Moreover, the terminal impedance of the altered distal vasculatures can be expressed more directly by changing the geometric parameters of the structure tree, such as the ratio of the daughter vessel radius to the parent one, or bifurcation generations. Therefore, the ST model is implemented as the outflow condition.

The topology of the ST model is presented in Fig. 2(d). Starting as a parent vessel, the terminal arteries with the radius of r_{p} bifurcate into two daughter vessels by α and β ($0 <$

α, $\beta < 1$), which means that the daughter vessels' radii reduce to αr_{p} and βr_{p}. The bifurcation ends until the radii of the daughter vessels are equal to the minimum radius.

Each segment of the small arteries can be considered as a resistance, and the bifurcated daughter vessels connect in parallel with the parent vessel. Thus, the impedance of the segments has the relationship of $\frac{1}{Z_{\mathrm{p}}} = \frac{1}{Z_{\mathrm{d1}}} + \frac{1}{Z_{\mathrm{d2}}}$. With the recursion algorithm from the bottom level of the structure tree to the top level, lastly, the whole impedance of the ST model $Z_{\mathrm{all}}(x, \omega)$ can be obtained. The outflow condition can be determined by a convolutional integral between the pressure and the inverse Fourier transform of the reciprocal value of impedance at the terminal arteries

$$Q(x, t) = \int_0^T P(x, \tau) Y(x, t - \tau)\, \mathrm{d}\tau, \tag{8}$$

where $Y(x, t) = \mathscr{F}^{-1}(1/Z_{\mathrm{all}}(x, \omega))$, and $\mathscr{F}^{-1}$ is the inverse Fourier transform operator. The more detailed derivations of the impedance of the ST model can be referred to Ref. [25].

2.3 0D AD model and its coupling with 1D model

To construct the 1D reduced model of FL, the FL is supposed to be a cylindrical tube, while the TL is still supposed to be a tapered tube. The length of FL is assumed to be equal to that of the TL. The flow in FL is controlled by the same system of Eqs. (2) and (3) as that in the TL. To take account of the blood flow through the tear, a 0D resistance model from Ref. [10] is added between the TL and the FL. The tear model is comprised of a resistance R ($\mathrm{Pa \cdot mL^{-1} \cdot s}$) expressed as

$$R = K \cdot A^b, \tag{9}$$

where $K = 47.42$, and $b = -1.2$, which are determined by the curve fitting of 8 clinical scenario data[10].

In the scenarios of our study, it is assumed that there are two tears with an entry and a re-entry, which are taken into account as a 0D model in two places. The cumulative tear impedes the flow between the FL and the TL, like in an electrical circuit, and the barrier effect is lumped in a resistance. As shown in Fig. 2(b), the flow through the tear causes a pressure drop as follows:

$$P_3 - P_4 = \Delta P = Q_3 R. \tag{10}$$

Compared with the bifurcation conditions of Eq. (7), the pressure drop through the entry and the re-entry has a further drop caused by the obstruction of the tear as follows:

$$P_1 = P_2 = P_3 = P_4 + \Delta P = P_4 + Q_3 R, \tag{11}$$

where the indices of 1, 2, and 3 represent the points before and after splitting into the TL and the FL, respectively, and 4 represents the starting point of the FL at the entry after the tear or the end point of FL at the re-entry in front of the tear. The blood flow rate through the entry and re-entry still has the same boundary condition as that at bifurcations, which is given by

$$Q_1 = Q_2 + Q_3. \tag{12}$$

2.4 Numerical methods

The inflow and outflow conditions are solved by the method of characteristics. Since the coupling condition between the 1D arterial tree and the AD model is similar to the bifurcation condition by adding an extra resistance, the Newton-Raphson procedure is employed in both coupling the AD with the 1D model and the bifurcation condition. Finally, the Lax-Wendroff method is applied to the discretization of Eqs. (2) and (3) with the second-order accuracy in both space and time. The following Courant-Friedrichs-Lewy (CFL) condition is satisfied:

$$\frac{\Delta t}{\Delta x} \leqslant \left| \frac{Q}{A} \pm c \right|^{-1}, \tag{13}$$

where Δt is the time step, Δx is length of the one dimensional mesh, and $c = \sqrt{\frac{A}{\rho}\frac{\partial P}{\partial A}}$ is the Moens-Korteweg pulse wave velocity which is linked to the vessel wall stiffness[16].

The program is developed from the open source code from the Github repository at https://github.com/updega2/StructuredTree.

2.5 WIA

WIA is increasingly used to analyze the wave propagation in practice recently, which can not only separate the wave into a forward wave and a backward wave but also show the wave intensity (WI)[23]. In WIA, the waves propagated in the arteries are considered by the sum of successive wavefronts $\mathrm{d}P_{\pm}$ for the pressure wave and $\mathrm{d}U\pm$ for the velocity wave, respectively, in which + denotes the forward wave and − denotes the backward wave.

Thanks to the hyperbolic feature of Eqs. (2) and (3), the pressure and velocity waves can be separated into forward and backward waves as

$$\mathrm{d}P_{\pm} = \frac{1}{2}(\mathrm{d}P \pm \rho c\,\mathrm{d}U), \tag{14}$$

and the velocity formula of the forward and backward waves are written as

$$\mathrm{d}U_{\pm} = \frac{1}{2}\Big(\mathrm{d}U \pm \frac{\mathrm{d}P}{\rho c}\Big). \tag{15}$$

Then, the intensities of the forward and backward waves can be calculated as

$$\mathrm{d}I_{\pm} \equiv \mathrm{d}P_{\pm}\,\mathrm{d}U_{\pm}. \tag{16}$$

Finally, the total WI can be expressed as

$$\mathrm{d}I = \mathrm{d}I_{+} + \mathrm{d}I_{-}. \tag{17}$$

The separated waveform can still be classified into two classes, i.e., compressed (positive $\mathrm{d}P$) and decompressed (negative $\mathrm{d}P$) waves. Hence, the waveform can be divided into four types, i.e., forward compressed wave (FCW), forward decompressed wave (FDW), backward compressed wave (BCW), and backward decompressed wave (BDW). Aortic WI profiles can exhibit the features of early ejection arising from ventricular contraction (FCW), late systole arising from ventricular relaxation (FDW), and vascular reflection of FCW (BCW). Thus, in the current study, the WIA in ascending aorta is especially focused on. The detailed derivations of WIA can be referred to Refs. [22] and [24].

All WIAs of the data for the control and AD groups are based on the computed results at the middle point of the ascending aorta, i.e., 2 cm away from the root of the ascending aorta (No. 1 in Table 2), for only the accumulative effect on the WI is the interest of this work.

3 Validation

To validate our 0D-1D coupling model, the flow profiles in FL by using our 0D-1D simulation and the MRI data from Ref. [10] are compared. The 0D-1D simulation is conducted by two different configurations of AD, i.e., the ideal model from Case 1 of Table 3 with the simplified inlet flow from Fig. 2(c) and the patient-specific model with geometric parameters of AD2 in Table 1 and a real inlet flow profile shown in Fig. 3(a)[29]. The results are shown in Fig. 3.

Rudenick et al.[10] pointed out that the FL flow patterns could be classified into four types, i.e., a systolic biphasic and primarily diastolic antegrade flow (named as BA, the systolic period is 0.43 s), a systolic biphasic and primarily diastolic retrograde flow (named as BR, the systolic period is 0.41 s), a systolic monophasic and primarily diastolic antegrade flow (named as MA, the systolic period is 0.39 s), and a systolic monophasic and primarily diastolic retrograde flow (named as MR, the systolic period is 0.33 s), as shown in Figs. 3(c) and 3(d).

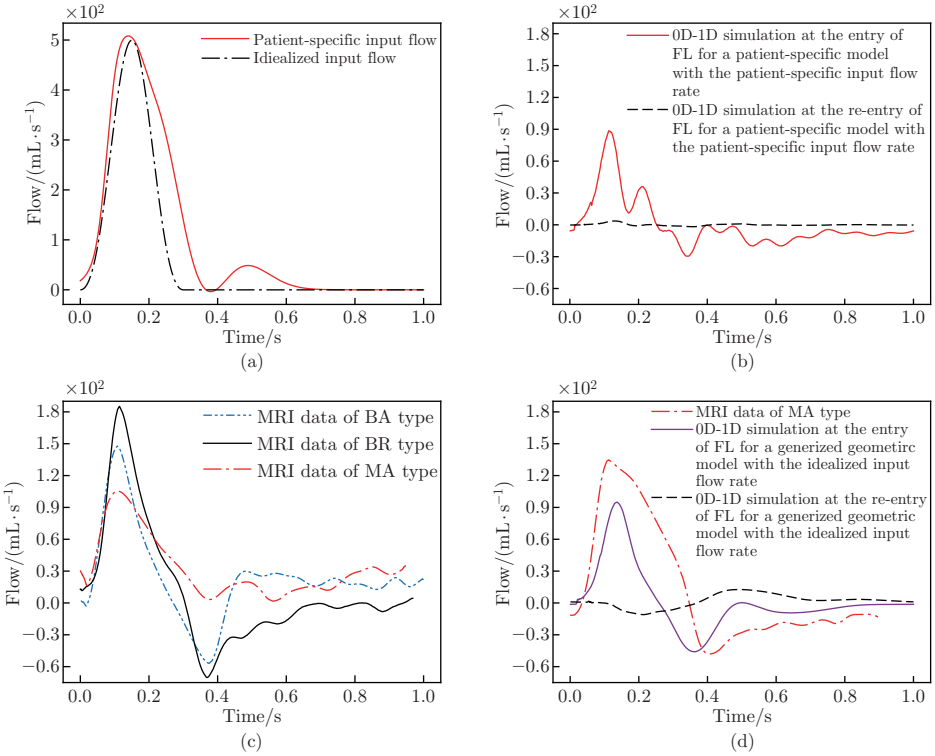

Fig. 3 Comparison of FL flows from Ref. [10] and 0D-1D simulation. (a) Inlet flow profile used for the patient-specific 0D-1D simulation of AD2 from Table 1 and idealized input flow for Case 1 in Table 3. (b) 0D-1D simulation results of the patient-specific AD model at the entry and re-entry of the FL. (c) Three measured flow patterns in the diaphragm region of FL by MRI from the literature. (d) 0D-1D simulation results of the ideal AD model at the entry and re-entry of the FL and one flow pattern in the diaphragm region of FL as MR from literature. (color online)

Table 3 Simulation AD cases

Case	Area of entry/mm^2	Area of re-entry/mm^2	Length of FL/mm	Equivalent radius of FL/mm
1	127	127 (100%)	250	10
2	127	12 (10%)	250	10
3	127	50 (40%)	250	10
4	127	180 (140%)	250	10
5	127	240 (190%)	250	10
6	127	180 (140%)	500	10
7	127	240 (190%)	500	10

It is seen that the 0D-1D results not only present retrograde flow at the end of the systolic period and with the same phase period in the flow wave, but also oscillate at the diastolic period. Besides, the flow wave for the real inlet waveform at the entry of the tear shows remarkable oscillations, whereas the one for the simplified inlet wave varies smoothly. There is a common feature that the simulated wave type in the entry of FL is similar to the MR or BR type of MRI data with the primarily diastolic retrograde flow[10], suggesting that the 1D simulation can capture the flow characteristics in FL under various inlet conditions. Furthermore, the flow pattern in FL highly depends on the inlet boundary condition and the configuration of tears.

To eliminate those effects, a single peak inlet flow profile is set in the subsequent simulation, and the proximal tear is fixed by changing the size and location of the distal tear.

4 Settings of the geometric data for the AD simulation

The geometric data of the simulation are based on the CT image data listed in Table 1, of which the average entry area and the equivalent radius of FL are around 127 mm^2 and 10 mm, respectively. Thus, as listed in Table 3, the entry area and the equivalent radius are fixed as 127 mm^2 and 10 mm, respectively. From Table 1, it can be seen that the FL has a constant radius but different lengths while the re-entry is at a different location in the distal segment. Besides, the re-entry size is considerably different from the entry size. In available literature, the distal tear has a dominant effect on hemodynamics. Therefore, the area size of the re-entry is set to be proportional to that of the corresponding entry in the simulation. The details of the simulation cases are listed in Table 3.

Before the AD simulation, a control group simulation of the healthy case without AD is conducted with the geometric parameters from Table 2.

5 Results

5.1 Flow and its distribution in the main arteries

Figure 4 gives the diagrams of the locations of the five arteries and the flow profiles in the middles of the five main arteries from the proximal to the distal and the contrast among the control case, Case 5, and Case 7. Figure 4(b) shows the reduction of the flow rate along the aorta from proximal to distal. It is seen that, compared with the the control case, in Cases 5 and 7, the flow rate considerably decreases from the thoracic aorta to the left femoral artery, the branch is exactly located in the area influenced by the lesion segment, and the flow rate in ascending aorta increases slightly.

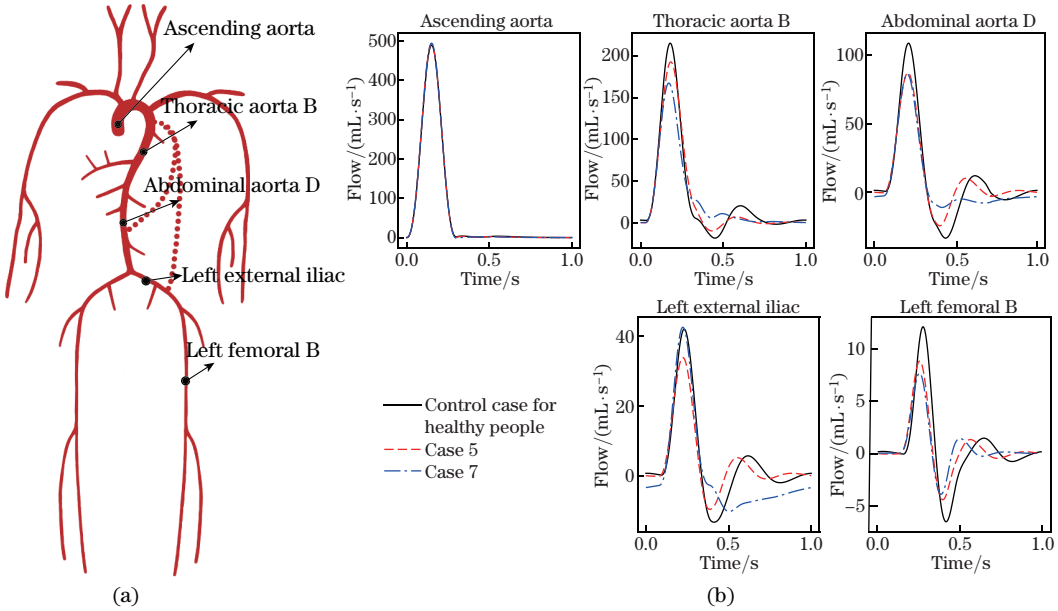

Fig. 4 (a) Locations of the five arteries in (b). (b) Flow profiles in the middles of the five main arteries from the proximal to the distal (color online)

Then, the blood flow waves for Cases 1–7 are computed by the 0D-1D model. The results are shown in Fig. 5, in which BF1 refers to the percentage of the mean flow rate into the thoracic aorta, BF2 refers to the ratio of the mean flow rate in superior mesenteric artery to that in abdominal aorta B, BF3 refers to the ratio of the mean flow rate in inferior mesenteric artery to that in abdominal aorta D, and BF4 refers to the ratio of the mean flow rate in left femoral artery B to that in left femoral artery A. In Fig. 5, the left column shows the mean flow rates of the parent arteries at four bifurcations (aortic arch B, abdominal aorta B, abdominal aorta D, and left femoral A), and the right column gives the blood flow ratios at the locations of four bifurcations (BF1, BF2, BF3, and BF4). It can be seen that the proximal bifurcation BF1 and the distal bifurcation BF4 are out of the FL, BF2 is inside the lesion segment both for the 25 cm- and 50 cm-length ADs, and BF3 is inside the lesion segment for the 50 cm-length AD but outside the FL for the 25 cm-length AD.

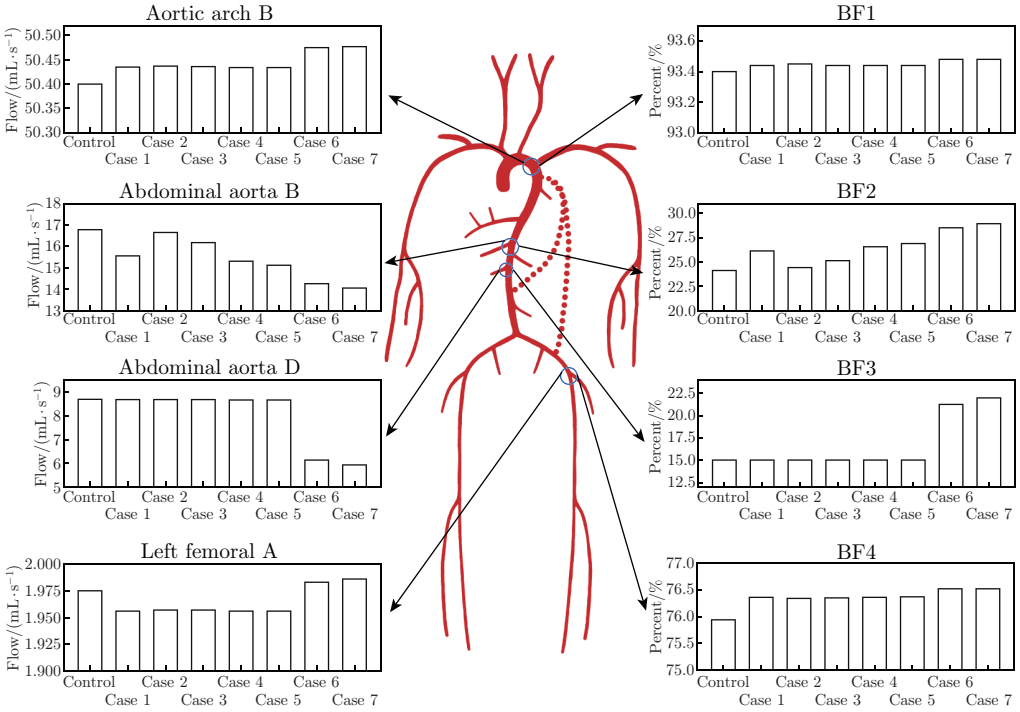

Fig. 5 Four flow distributions (BF1, BF2, BF3, and BF4) and the mean flow rates at the ends of the parent arteries of four bifurcations (aortic arch B, abdominal aorta B, abdominal aorta D, and left femoral A) for the control case and Cases 1–7. The flow distribution ratio is defined by Percent (%) $= Q_{\mathrm{d}}/Q_{\mathrm{p}} \times 100\%$, where Q_{d} is the mean flow at the start of one of the daughter arteries and Q_{p} is the mean flow at the end of the parent artery. The daughter arteries for the four bifurcations are the thoracic aorta, the superior mesenteric artery, the inferior mesenteric artery, and the left femoral artery B, while the parent arteries for the four bifurcations are the aortic arch B, the abdominal aorta B, the abdominal aorta D, and the left femoral artery A (color online)

From the right graphs of Fig. 5, it can be seen that the flow distribution ratios for all the 7 cases at BF1 and BF4 increase up to 0.08% and 0.58% compared with the control case. Since BF1 and BF4 are out of the lesion segment, the flow distributions are virtually unaffected. At BF3, the flow distribution ratios in Cases 6 and 7 increase 6.24% and 6.97% compared with that of the control case, respectively. Under the same flow condition, the flow distribution

ratios at BF3 in Cases 1–5 are the same as that for the control case. This difference is closely associated with the relative position between BF3 and FL. In Cases 6 and 7, BF3 is inside the FL segment. However, it is outside the FL-segment for Cases 1–5. Moreover, at BF2, the flow distribution ratios increase with the distal tear size from Cases 1–5. Further comparisons of the flow distribution ratios at BF2 for Cases 4–7 reveal that the longer FL also results in the increase in the flow distribution ratio. The left graphs of Fig. 5 present the mean flow rates at the outlet of the parent arteries of BF1, BF2, BF3, and BF4. The results show that at abdominal aorta B and abdominal aorta D, the mean flow rates for Cases 1–7 are less than that for the control case. Compared with the control case, for Case 7, the maximum reduction of the mean flow is 16.25% at abdominal aorta B, and even reaches 31.74% at abdominal aorta D. However, compared with the control case, the maximum relative changes do not exceed 1% at abdominal aorta D for Cases 1–5, aortic arch for Cases 1–7, and left femoral A for Cases 1–7.

Figure 6 shows the WIs of the decomposed forward and backward waves for the control case and Cases 2, 5, and 7. There are two peaks in the forward wave, i.e., FCW and FDW, while there is only one peak in the backward wave, i.e., BCW[22–23]. Compared with the three waves in the control group shown in Fig. 6(a), the FCWs increase by 8.90% for

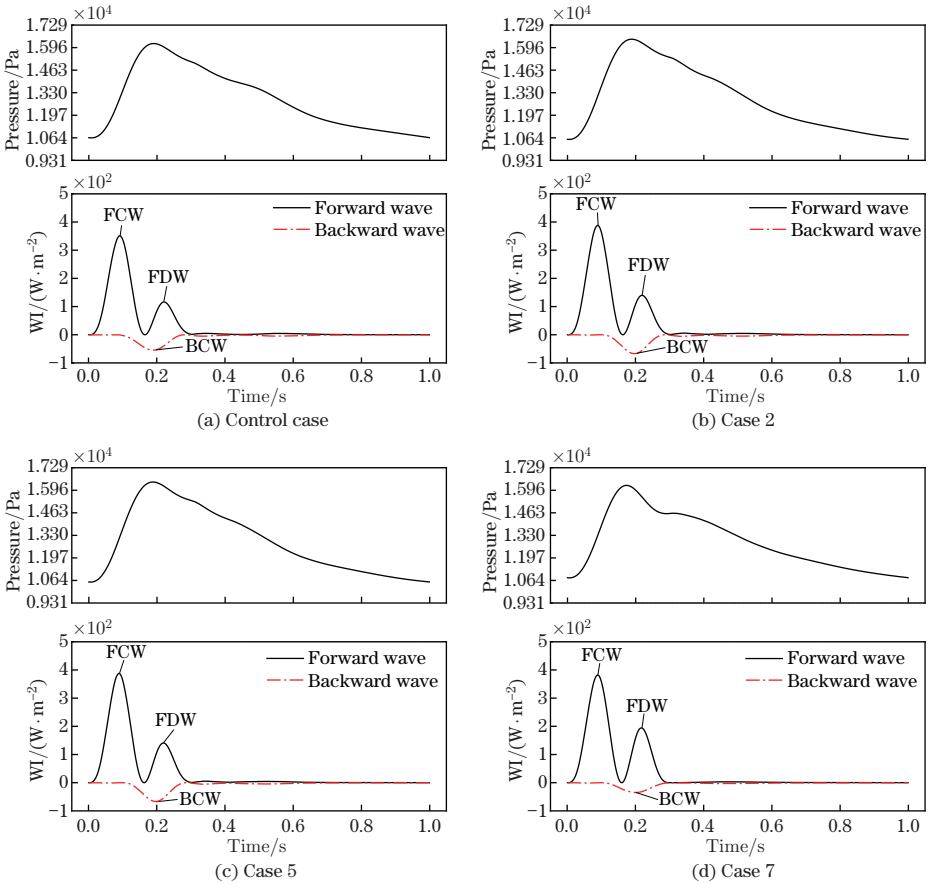

Fig. 6 Decomposed wave intensities at the middle of ascending aorta for the control case and Cases 2, 5, and 7. The pressure waveforms are shown on the top of the WI profiles. When the pressure increases, the wave is a compressed one; while when the pressure decreases, the wave is a decompressed one (color online)

Cases 2 and 5 while 7.9% for Case 7. Meanwhile, the FDW for Case 7 shows a considerable increase by nearly 56%, whereas the FDWs for Cases 2 and 5 solely rise by 18%. In contrast, the BCWs for Cases 2, 5, and 7 show opposite variation tendencies, among which the BCWs increase by 18% for Cases 2 and 5 but by 44.5% for Case 7. The results show that AD leads to the increases in FCW and FDW simultaneously, but the increase is more remarkable for FDW in AD with a longer FL. The results also show that compared with the control case, the systolic pressure increases slightly for Cases 2 and 5 but decreases slightly with a distinct reflection wave for Case 7 (see Fig. 6(d)).

5.2 Flow patterns in FL from the proximal to the distal

Figure 7 presents the flow waves in FL for Cases 1–7 from the proximal to the distal. It is seen that the flow profiles along the flow direction in all cases present similar variational tendencies. At the proximal of the FL entry, the wave is positive and then negative. With the increase in the distance to the entry, the flow waveforms become gradually damping. Especially, at the distal of the entry, i.e., at the re-entry, the flow switches to be a retrograde one with a negative peak first, and then changes to be a positive wave with oscillations. The computed flow patterns are in favorable agreement with those of Rudenick et al.[10]. Among them, the feature of the retrograde flow is the most indistinct for Case 2 with the smallest size of the re-entry. In Case 5, there is the most retrograde flow for the biggest re-entry area.

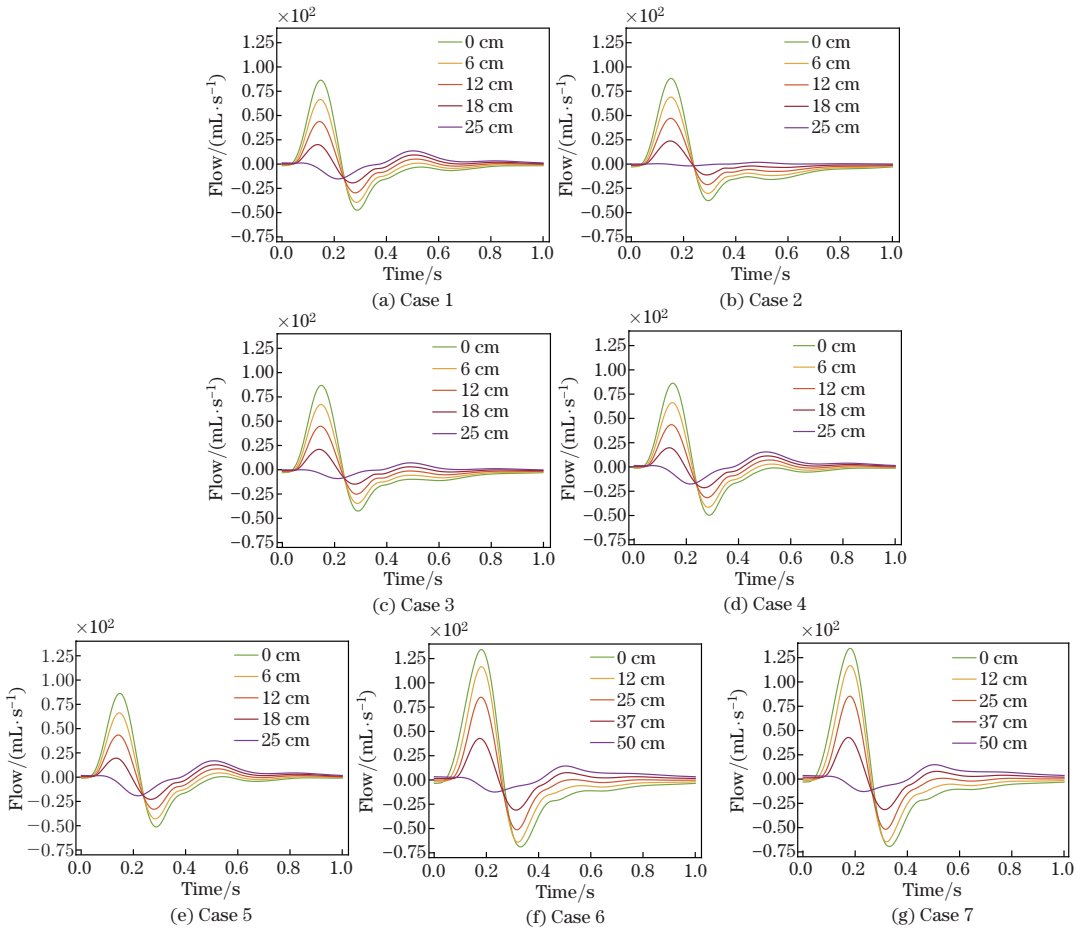

Fig. 7 Flow patterns along the FL at five locations with five colored lines from the entry to the re-entry (color online)

The pressure difference of FL and TL can provide the information of flow variations in FL and the movement of the intimal flap in detail. Figure 8 shows the pressure difference between FL and TL along the flow direction for Cases 2, 5, and 7. The pressure difference in this work is defined as the pressure waveform in FL minus the pressure waveform in TL at one location. It is seen that the pressure difference has a negative peak first and then a positive peak in a period, has the largest value at the entry, and gradually decreases with the increase in the distance to the entry.

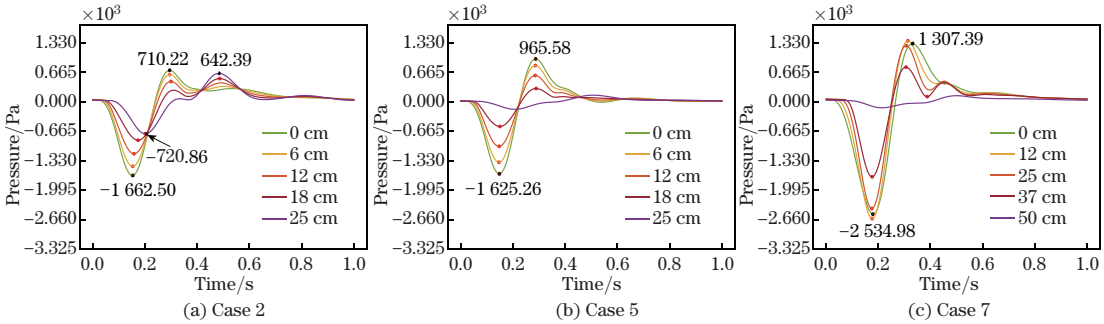

(a) Case 2 (b) Case 5 (c) Case 7

Fig. 8 Pressure difference between FL and TL along the longitude at five locations for Cases 2, 5, and 7 (color online)

In order to present the pressure difference between FL and TL, Fig. 9 gives the pressure waveforms of FL and TL at the position 12 cm away from the entry of the lesion segment for Cases 2, 5, and 7. It is observed that there is a phase shift in the pressure waveform between FL and TL, implying that there is a delay of pressure waveform in FL compared with that in TL. Among the three cases, Case 7 presents the most distinct phase delay.

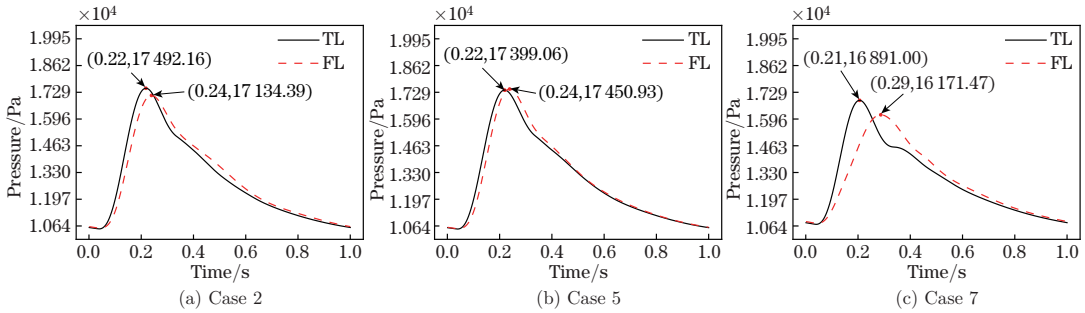

(a) Case 2 (b) Case 5 (c) Case 7

Fig. 9 Pressure profiles in FL and TL at the position 12 cm away from the entry for Cases 2, 5, and 7 (color online)

6 Discussion

Since the 1D system of Eqs. (2) and (3) is hyperbolic, the wave propagation can be analyzed. It is the first time to apply 1D modeling to studying wave propagation in the cardiovascular system with AD though 1D modeling has been widely used in hypertension, cerebral cycle, and coronary cardiovascular system access[18, 20, 24].

The computational results show that the flow in FL matches well with the MRI data from Ref. [10] (see Fig. 3), where the retrograde flows and the flow oscillation in FL are captured with slightly smaller peak values of the flow waveform in FL. The computed flow pattern in FL can be classified as MR or BR[10] according to the differences of the flow characteristics at the systolic and diastolic periods. Moreover, the 0D-1D model provides the blood flow characteristics immediately, which can give a fast clinical auxiliary diagnosis. The advantage

of 3D simulation is that it can provide more invaluable information about the local flow field such as the wall shear stress (WSS) distribution, the oscillatory index (OSI) distribution, and the flap movement of AD. Nevertheless, considering the computational time cost, among 0D, 1D, and 3D models, 1D model has the greatest potential in both cardiovascular research and clinical practice[13].

According to the geometric parameters of AD in Table 1, two degrees of TBAD are defined. One is that the FL volume is around 50 000 mm^2, while the other two volumes range from 200 000 mm^2 to 240 000 mm^2. It is interesting to note that the entry area is either nearly equal to, double, or half of the re-entry area. Thus, in the simulation, the size and position of the entry at the proximal thoracic aorta are fixed, the re-entry is set at two positions mimicking the two degrees of TBAD. Consequently, the studies on the effect of the distal tear are implemented by varying the distal tear size and location shown in Table 3.

6.1 Effect of AD on the wave propagation in the cardiovascular system from the proximal to the distal

Figure 4(b) clearly shows that the peak values of the waveform in the ascending aorta for Cases 5 and 7 are a little higher than those of the control case, whereas the flow waveforms at the bifurcated branches in the AD involved segments shows a remarkably smaller amplitude than that for the control case. The mean flow rates shown in the left graphs of Fig. 5 present the same tendency as that shown in Fig. 4(b).

The appearance of AD causes not only the increase in the flow peak in the ascending aorta but also the reinforcement of the forward WI. According to the WI theory[20, 30], the increased WI of the FCW indicates the morphological change of proximal vessels. Since the FCW is caused by the ventricular ejection and acceleration of the aortic blood flow, the physical sense of WI is the blood flow power, and the WI depends on the interaction of heart and load[23–24], the increased WIs in FCWs imply a larger load on the heart for blood ejection. Meanwhile, it is inferred that the longer FL can eliminate more influence of wave reflection than the shorter FL. Besides, the WI can be used as the index for the evaluation of the severity of AD. The elevation of FDWs for Cases 1–7 suggests the deceleration of ventricular contraction before the closure of the aortic valve. The increase in the WI for the forward wave means that AD can result in an overload in the heart and longer FL can balance more impedance from the distal sites. The latest studies based on clinic data could give some evidence. In 68 TAAD patients, the values of the left ventricular ejection fraction (LVEF) for 13 subjects were less than 50%[31]. In TAAD patients, the LVEF of 29.1% was below the lower limit of 52% for females and 54% for males, suggesting left ventricular dysfunction in the patients[32]. Since retrograde flow is the common feature for TAAD and TBAD, TBAD can also have an impact on ventricular ejection. It is suggested from the modeling work that we should pay close attention to the left ventricular dysfunction caused by type B even if there are not many published studies now.

6.2 TL ischemia

The 0D-1D coupling simulation of the cardiovascular system can show the global features of flow variations in TBAD. From the right graphs of Fig. 5, it is seen that the flow distribution in the bifurcations changes significantly when the bifurcations are located within the region of the lesion vessel segment. In contrast, the flow distribution nearly keeps constant when the bifurcation is out of the injured segment, no matter whether the bifurcation is at the proximal or distal end. Even in Cases 6 and 7, where BF4 is closer to the re-entry than in Cases 1–5, there are no distinct variations for the flow ratio compared with the control case. Similar situations can be noted for BF1 where the bifurcation is near the entry but outside the lesion segment. However, the flow ratio to BF2 increases with the area of distal tear from Cases 1 to 7, suggesting that more blood flows into the superior mesenteric artery and less blood flows into another daughter branch. For BF3, Cases 1–5 and the control group are practically the same, since BF3 is inside the influenced region of the lesion segment. For Cases 6 and 7, since the bifurcation is included in the lesion segment, the flow ratio remarkably increases. The flow

distribution characteristics at BF2 and BF3 also show that longer FL can further cause the redistribution at the bifurcations, leading to less blood flow in the main branch. In summary, the results infer that TBAD can affect the flow distribution in the region within the lesion segment, but has a less effect on the flow distribution outside the lesion segment. Moreover, for abdominal aorta B, the mean flow rate decreases for all the 7 cases. Using the mean flow of abdominal aorta B to multiply the flow distribution ratio at BF2, we find out that the mean flow rates of the secondary daughter artery almost keep the same from Cases 1–7. The results induce less blood flow into the other daughter artery, e.g., abdominal aorta C. The same reduction of blood flow rate in abdominal aorta E may occur since the ratio at BF3 increases as well for the 7 cases. These results suggest that ischemia will occur in TL and may further lead to compression of TL[33].

6.3 Interaction between TL and FL

The common feature of the flow profiles in FL is that there are two flow peaks, first a positive one and then a negative one, which reduce from the proximal to the distal gradually. In contrast to other places in FL, near the re-entry, a retrograde flow appears, followed by an anterograde flow. Therefore, FL performs like a pump doing a suction-expulsion movement. In other words, blood flows into the FL through two tears during the systolic phase with a delay of flow at the re-entry and flows out of FL through the two tears during the diastolic phase. This pumping-like phenomenon has also been reproduced by 3D simulation[34]. The retrograde flow in TBAD may be associated with the retrograde tearing to develop into TAAD due to its long-term outcome influence[7]. However, the 'pumping-like' phenomenon becomes weakened with the length of FL because the anterograde flow is strengthened (see Figs. 7(d)–7(g)).

In addition, the intimal flap, which separates the lumen into TL and FL, has a notable movement in the cardiac cycle observed via CT imaging[28]. It is found that the intimal flap is unfilled toward FL at the systolic period, but unfilled toward TL at the diastolic period. Using fluid-structure interaction, more insights into the intimal flap movement have been achieved. Keramati et al.[35] showed that the temporal waveform of the pressure difference between FL and TL corresponded to the drastic intimal flap movement exactly. Chong et al.[36] captured the drastic temporal flap movement and pressure difference between FL an TL by using an efficient fluid-structure coupling strategy. Xu et al.[37] used the pressure difference as an indicator for the assessment of the severity of TBAD and functional improvement after TEVAR, and obtained that the position of the zero point of the pressure difference shifted downward along the aorta. From Fig. 8, it is observed that the pressure difference waveforms also show that the pressure is larger in TL than in FL at the systolic period, indicating that the intimal flap moves to the FL side at systolic phase. In contrast, the pressure is larger in FL than in TL at the diastolic period, indicating that the intimal flap moves to the TL side during the diastolic phase. Moreover, there are larger peaks on the pressure difference near the entry among all the 7 cases, which suggests a greater displacement of the intimal flap at the proximal of the lesion segment. The larger FL pressure is also observed and simulated in Ref. [38], and there is the suggestion of restraining the movement of the intimal flap.

For wave propagation, the reasons for the generation of nonzero pressure difference are twofold. On the one hand, the pressure wave in FL has a delay compared with that in TL (see Fig. 9). On the other hand, the peak value of the pressure in FL is smaller than the one in TL (see Figs. 9(a) and 9(c)). When blood flows into the FL through the entry, the tear impedes the flow, which results in the first delay of the wave. Then, the reflected wave from the distal enters the FL through the re-entry, causing a second delay. The delay of the pressure wave between FL and TL is the integrated effect of the two delays mentioned above. Comparing Case 2 with Case 5 in Fig. 9, it is observed that the smaller re-entry tear leads to a smaller peak of pressure in FL. Rudenick et al.[2] has reported that the effect of reduction on the FL pressure is caused by the decrease in the tear. Additionally, longer FL also reduces the pressure peak since larger compliance corresponds to larger volume of FL.

6.4 Effect of distal tear on hemodynamics

Prior studies have shown the importance of tear size in AD, but most of them focused on the influence of the proximal tear. In this study, the influence of the distal tear has been studied comprehensively. The obstruction effect on blood between FL and TL can be seen from Figs. 7(a)–7(c). Since Cases 2 and 3 have 10% and 40% of the distal tear size as that of Case 1, the flow profiles are damping at the distal tear in Cases 2 and 3, and there are nearly no flow rates at the re-entry, causing the flow exchange between FL and TL only through the entry in Cases 2 and 3. The flow profiles in Cases 4 and 5 indicate that the bigger the distal tear is, the stronger the retrograde flow becomes. In contrast, the increment of the distal tear does not lead to much increase in the flow rate in FL (see Figs. 7(d) and 7(e)). This can be explained from Eq. (10) that the tear size almost has no significant influence on the resistance at larger tear size. Comparing Case 2 with Case 5 in Fig. 9, it is observed that the smaller re-entry tear leads to a smaller peak of pressure in FL. This result agrees well with the result of Rudenick et al.[2]. Rudenick et al.[2] also pointed out that smaller tears resulted in a larger pressure difference between FL and TL, which is consistent with our results in Figs. 8(a) and 8(b). Additionally, longer FL also decreases the peak of pressure (see Fig. 9(c)). Canchi et al.[39] pointed out that a large distal tear was an overall significant factor influencing FL dilation, which might correspond to the stronger retrograde flow led by the larger distal tear. Our study also confirms the greater possibility of thrombosis for the smaller distal tear showing that the distal flow is extremely small for easy thrombosis[40]. All the results show that the distal tear also requires more attention.

7 Limitations and prospect

Despite the local and global characteristics of flow in TBAD revealed by using the 0D-1D model, there are still some limitations in this study. First, the single peak inlet flow profile and the generic data of arteries are used in our 0D-1D simulation, which cannot perform a variety of flow profiles in FL according to the MRI data from Rudenick et al.[2]. In the simulation of this work, Young's modulus of healthy vessel walls is employed. However, the mechanical properties of vessel walls are more complicated for AD aorta. In an in-vitro study[41], it is observed that there are a lot of fatty materials between the intimal and median layers, which may bring effects on the properties of the AD vessel wall. The image-based assessment of mechanical properties of various vessel walls may be helpful for understanding the mechanical properties under the pathological conditions of the vessel walls.

Besides, the movement of the intimal flap between TL and FL through the intimal flap has been neglected. If we want to simulate the movement of the intimal flap by 1D model, we may change the expression of Eq. (4) by adding the influence of pressure variation on the other side of the flap. Though our model can shed light on the intimal flap shape in the systolic and diastolic phases indirectly by the pressure difference between FL and TL, the real intimal flap movement is not modeled since TL and FL are considered as two individual tubes. Moreover, the spatial information of the spiral structure of FL along the TL observed in many situations is lost. One possible solution is using more MRI data for fitting a more precise lumped-parameter model, such as adding new elements in the lumped-parameter model. Additionally, the tear model from Ref. [10] is a primary model for only 8 measured data. More simulation and measurements are needed to investigate the effects of the tear features on the pressure drop across the tear for the development of a more comprehensive formula. Currently, only two-tear situations are simulated in this work. In clinic situation, tears frequently appear in patients. For the one-tear situation, we can occlude one end of FL and apply a reflecting boundary condition[16]. While using the same way dealing with the two-tear condition, the current 1D model can be extended to analyze the flow with multiple tears.

8 Conclusions

In this work, a 0D-1D cardiovascular system model is presented to study the flow characteristics in the cardiovascular system with TBAD. The simulated flow waveforms in FL show the oscillation and retrograde characteristics, which agree well with the data from the literature. Our results show that the WI can be used as an accessory index of the degree of FL. A smaller distal tear results in a smaller retrograde flow and a higher pressure difference since a smaller distal tear can restrain the pumping-like movement of FL. In contrast, a larger distal tear can induce a remarkable retrograde flow, which may be associated with the development of type B into more severe dissection at the proximal end. At the same time, a larger pressure difference between FL and TL is observed for a larger distal tear, indicating a stronger interplay between FL and TL at the re-entry. It is also confirmed that the pressure difference between FL and TL is due to the phase lag of pressure waves in the two lumens. The occurrence of AD has effects on the flow distributions in the branches within the influenced region of the injured segment, but has nearly no influence on those of the branches outside the lesion segment. The 0D-1D modeling can provide a fast system simulation of the cardiovascular system with altered flow waveforms, flow distributions, and further assessment of ischemia in the main organs and left ventricular ejection function in AD patients, showing potential applications for future clinical auxiliaries.

References

[1] LIU, L., ZHANG, S., LU, Q. S., JING, Z. P., ZHANG, S. M., and XU, B. Impact of oversizing on the risk of retrograde dissection after tevar for acute and chronic type B dissection. *Journal of Endovascular Therapy*, **23**, 620–625 (2016)

[2] RUDENICK, P. A., BIJNENS, B. H., GARCÍA-DORADO, D., and EVANGELISTA, A. An in vitro phantom study on the influence of tear size and configuration on the hemodynamics of the lumina in chronic type B aortic dissections. *Journal of Vascular Surgery*, **57**, 464–474 (2013)

[3] EVANGELISTA, A., GALUPPO, V., GRUOSSO, D., CUÉLLAR, H., TEIXIDÓ, G., and RODRÍGUEZ-PALOMARES, J. Role of entry tear size in type B aortic dissection. *Annals of Cardiothoracic Surgery*, **3**, 403–405 (2014)

[4] TSAI, T. T., SCHLICHT, M. S., KHANAFER, K., BULL, J. L., VALASSIS, D. T., WILLIAMS, D. M., BERGUER, R., and EAGLE, K. A. Tear size and location impacts false lumen pressure in an ex vivo model of chronic type B aortic dissection. *Journal of Vascular Surgery*, **47**, 844–851 (2008)

[5] WEISS, G., WOLNER, I., FOLKMANN, S., SODECK, G., SCHMIDLI, J., GRABENWÖGER, M., CARREL, T., and CZERNY, M. The location of the primary entry tear in acute type B aortic dissection affects early outcome. *European Journal of Cardio-Thoracic Surgery*, **42**, 571–576 (2012)

[6] CHI, Q. Z., CHEN, H. M., MU, L. Z., HE, Y., and LUAN, Y. Haemodynamic analysis of the relationship between the morphological alterations of the ascending aorta and the type A aortic-dissection disease. *Fluid Dynamics & Materials Processing*, **17**, 721–743 (2021)

[7] AL-KALEI, A., WU, Z. H., and ZHANG, H. K. Influence of primary intimal tear location in type B aortic dissection as a factor portending retrograde type A aortic dissection after endovascular repair. *Journal of vascular and Interventional Radiology*, **29**, 833–840 (2018)

[8] SUN, Z. H. and CHAICHANA, T. A systematic review of computational fluid dynamics in type B aortic dissection. *International Journal of Cardiology*, **210**, 28–31 (2016)

[9] AB NAIM, W. N. W., GANESAN, P. B., SUN, Z. H., CHEE, K. H., HASHIM, S. A., and LIM, E. A perspective review on numerical simulations of hemodynamics in aortic dissection. *The Scientific World Journal*, **2014**, 652520 (2014)

[10] RUDENICK, P. A., SEGERS, P., PINEDA, V., CUELLAR, H., GARCÍA-DORADO, D., EVANGELISTA, A., and BIJNENS, B. H. False lumen flow patterns and their relation with morphologi-

cal and biomechanical characteristics of chronic aortic dissections. computational model compared with magnetic resonance imaging measurements. *PLoS One*, **12**, e0170888 (2017)

[11] REYMOND, P., MERENDA, F., PERREN, F., RÜFENACHT, D., and STERGIOPULOS, N. Validation of a one-dimensional model of the systemic arterial tree. *American Journal of Physiology-Heart and Circulatory Physiology*, **297**, H208–H222 (2009)

[12] BOILEAU, E., NITHIARASU, P., BLANCO, P. J., MÜLLER, L. O., FOSSAN, F. E., HELLEVIK, L. R., DONDERS, W. P., HUBERTS, W., WILLEMET, M., and ALASTRUEY, J. A benchmark study of numerical schemes for one-dimensional arterial blood flow modelling. *International Journal for Numerical Methods in Biomedical Engineering*, **31**, e02732 (2015)

[13] LIU, H., LIANG, F. Y., WONG, J., FUJIWARA, T., YE, W. J., TSUBOTA, K., and SUGAWARA, M. Multi-scale modeling of hemodynamics in the cardiovascular system. *Acta Mechanica Sinica*, **31**, 446–464 (2015)

[14] STERGIOPULOS, N., YOUNG, D. F., and ROGGE, T. R. Computer simulation of arterial flow with applications to arterial and aortic stenoses. *Journal of Biomechanics*, **25**, 1477–1488 (1992)

[15] FORMAGGIA, L., LAMPONI, D., and QUARTERONI, A. One-dimensional models for blood flow in arteries. *Journal of Engineering Mathematics*, **47**, 251–276 (2003)

[16] FORMAGGIA, L., LAMPONI, D., TUVERI, M., and VENEZIANI, A. Numerical modeling of 1D arterial networks coupled with a lumped parameters description of the heart. *Computer Methods in Biomechanics and Biomedical Engineering*, **9**, 273–288 (2006)

[17] MYNARD, J. P. and SMOLICH, J. J. One-dimensional haemodynamic modeling and wave dynamics in the entire adult circulation. *Annals of Biomedical Engineering*, **43**, 1443–1460 (2015)

[18] VAN DE VOSSE, F. N. and STERGIOPULOS, N. Pulse wave propagation in the arterial tree. *Annual Review of Fluid Mechanics*, **43**, 467–499 (2011)

[19] COCCARELLI, A., PRAKASH, A., and NITHIARASU, P. A novel porous media-based approach to outflow boundary resistances of 1D arterial blood flow models. *Biomechanics and Modeling in Mechanobiology*, **18**, 939–951 (2019)

[20] ZHANG, X. C., LIU, J., CHENG, Z. H., WU, B. K., XIE, J., ZHANG, L., ZHANG, Z. J., and LIU, H. Personalized 0D-1D multiscale hemodynamic modeling and wave dynamics analysis of cerebral circulation for an elderly patient with dementia. *International Journal for Numerical Methods in Biomedical Engineering*, **37**, e3510 (2021)

[21] TOMASI, J., BARS, F. L., SHAO, C., LUCAS, A., LEDERLIN, M., HAIGRON, P., and VERHOYE, J. P. Patient-specific and real-time model of numerical simulation of the hemodynamics of type B aortic dissections. *Medical Hypotheses*, **135**, 109477 (2020)

[22] PARKER, K. H. An introduction to wave intensity analysis. *Medical & Biological Engineering & Computing*, **47**(2), 175–188 (2009)

[23] WESTERHOF, N., SEGERS, P., and WESTERHOF, B. E. Wave separation, wave intensity, the reservoir-wave concept, and the instantaneous wave-free ratio: presumptions and principles. *Hypertension*, **66**, 93–98 (2015)

[24] MYNARD, J. P. *Computer Modelling and Wave Intensity Analysis of Perinatal Cardiovascular Function and Dysfunction*, Ph. D. dissertation, University of Melbourne, Melbourne (2011)

[25] OLUFSEN, M. S., PESKIN, C. S., KIM, W. Y., PEDERSEN, E. M., NADIM, A., and LARSEN, J. Numerical simulation and experimental validation of blood flow in arteries with structured-tree outflow conditions. *Annals of Biomedical Engineering*, **28**, 1281–1299 (2000)

[26] GUAN, D. B., LIANG, F. Y., and GREMAUD, P. A. Comparison of the Windkessel model and structured-tree model applied to prescribe outflow boundary conditions for a one-dimensional arterial tree model. *Journal of Biomechanics*, **49**, 1583–1592 (2016)

[27] HE, Y., LIU, H., and HIMENO, R. A one-dimensional thermo-fluid model of blood circulation in the human upper limb. *International Journal of Heat and Mass Transfer*, **47**, 2735–2745 (2004)

[28] BONFANTI, M., BALABANI, S., GREENWOOD, J. P., PUPPALA, S., HOMER-VANNIASINKAM, S., and DÍAZ-ZUCCARINI, V. Computational tools for clinical support: a multi-scale compliant model for haemodynamic simulations in an aortic dissection based on multi-modal imaging data. *Journal of the Royal Society Interface*, **14**, 20170632 (2017)

[29] MORBIDUCCI, U., PONZINI, R., GALLO, D., BIGNARDI, C., and RIZZO, G. Inflow boundary conditions for image-based computational hemodynamics: impact of idealized versus measured velocity profiles in the human aorta. *Journal of Biomechanics*, **46**, 102–109 (2013)

[30] HUGHES, A. D., PARKER, K. H., and DAVIES, J. E. Waves in arteries: a review of wave intensity analysis in the systemic and coronary circulations. *Artery Research*, **2**, 51–59 (2008)

[31] LI, Y. L., GAO, Q. Y., FENG, J. B., ZHANG, C. X., and GE, S. L. The death risk factors of stanford A aortic dissection surgery (in Chinese). *Chinese Journal of General Practice*, **20**, 18–21 (2022)

[32] THURAU, J., HABAZETTL, H., AL, A. A., MLADENOW, A., ZASCHKE, L., ADAM, U., KUPPE, H., WUNDRAM, M., KUKUCKA, M., and KURZ, S. D. Left ventricular systolic dysfunction in patients with type-A aortic dissection is associated with 30-day mortality. *Journal of Cardiothoracic and Vascular Anesthesia*, **33**, 51–57 (2019)

[33] CHUNG, J. W., ELKINS, C., SAKAI, T., KATO, N., VESTRING, T., SEMBA, C. P., SLONIM, S. M., and DAKE, M. D. True-lumen collapse in aortic dissection. *Radiology*, **214**, 99–106 (2000)

[34] BIRJINIUK, J., TIMMINS, L. H., YOUNG, M. M., LESHNOWER, B. G., OSHINSKI, J. N., KU, D. N., and VEERASWAMY, R. K. Pulsatile flow leads to intimal flap motion and flow reversal in an in vitro model of type B aortic dissection. *Cardiovascular Engineering and Technology*, **8**, 378–389 (2017)

[35] KERAMATI, H., BIRGERSSON, E., HO, J. P., KIM, S., CHUA, K. J., and LEO, H. L. The effect of the entry and re-entry size in the aortic dissection: a two-way fluid-structure interaction simulation. *Biomechanics and Modeling in Mechanobiology*, **19**, 2643–2656 (2020)

[36] CHONG, M. Y., GU, B., CHAN, B. T., ONG, Z. C., XU, X. Y., and LIM, E. Effect of intimal flap motion on flow in acute type B aortic dissection by using fluid-structure interaction. *International Journal for Numerical Methods in Biomedical Engineering*, **36**, e3399 (2020)

[37] XU, H. M., XIONG, J., HAN, X. F., MEI, Y. Q., SHI, Y., WANG, D. P., ZHANG, M. C., and CHEN, D. D. Computed tomography-based hemodynamic index for aortic dissection. *Journal of Thoracic and Cardiovascular Surgery*, **162**, e165–e176 (2021)

[38] PEELUKHANA, S. V., WANG, Y., BERWICK, Z., KRATZBERG, J., KRIEGER, J., ROEDER, B., CLOUGH, R. E., HSIAO, A., CHAMBERS, S., and KASSAB, G. S. Role of pulse pressure and geometry of primary entry tear in acute type B dissection propagation. *Annals of Biomedical Engineering*, **45**, 592–603 (2017)

[39] CANCHI, S., GUO, X. M., PHILLIPS, M., BERWICK, Z., KRATZBERG, J., KRIEGER, J., ROEDER, B., HAULON, S., CHAMBERS, S., and KASSAB, G. S. Role of re-entry tears on the dynamics of type B dissection flap. *Annals of Biomedical Engineering*, **46**, 186–196 (2017)

[40] LI, D., ZHENG, T. H., LIU, Z., LI, Y., YUAN, D., and FAN, Y. B. Influence of distal re-entry tears on false lumen thrombosis after thoracic endovascular aortic repair in type B aortic dissection patients: a computational fluid dynamics simulation. *Cardiovascular Engineering and Technology*, **12**, 426–437 (2021)

[41] CHI, Q. Z., GE, Y. Y., MU, L. Z., CAO, Z., LONG, L. L., LUAN, Y., and HE, Y. In vitro experimental study of true and false lumen based on aortic dissection silicone model and CT angiography (in Chinese). *Journal of Medical Biomechanics*, **36**, 443 (2022)